Acid-Base Chemistry of a Model IrO_2 Catalytic Interface

Abhinav S. Raman and Annabella Selloni*

Department of Chemistry, Princeton University, Princeton, NJ 08544, USA

E-mail: aselloni@princeton.edu

Abstract

Iridium oxide (IrO_2) is one of the most efficient catalytic materials for the oxygen evolution reaction (OER), yet the atomic scale structure of its aqueous interface is largely unknown. Herein, the hydration structure, proton transfer mechanisms and acid-base properties of the rutile IrO_2(110)-water interface are investigated using *ab-initio* based deep neural-network potentials and enhanced sampling simulations. The proton affinities of the different surface sites are characterized by calculating their acid dissociation constants, which yield a point of zero-charge in good agreement with experiments. A large fraction ($\approx$ 80%) of adsorbed water dissociation is observed, together with a short lifetime ($\approx$ 0.5 ns) of the resulting terminal hydroxy groups, due to rapid proton exchanges between adsorbed H_2O and adjacent OH species. This rapid surface proton transfer supports the suggestion that the rate-determining step in the OER may not involve proton transfer across the double layer into solution, as indicated by recent experiments.

TOC Graphic

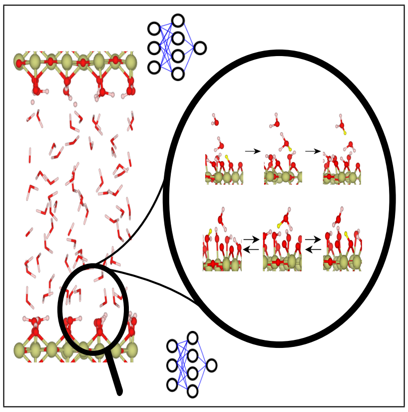

Electrocatalytic water-splitting has been one of the most sought after routes for the sustainable production of "green" hydrogen over the past decade.[1,2] The oxygen evolution reaction (OER), presents the largest bottleneck in this process, owing to its sluggish kinetics resulting in major energy losses.[1–5] Thus far, IrO_2 has been the only viable catalyst for the OER, due to its good activity and reasonable stability under the typically acidic operating conditions encountered in proton exchange membrane (PEM) electrolyzers.[2–8] Research efforts, both experimental and computational, have therefore intensely targeted the improvement of catalytic activity guided by physical descriptors.[1,9–18] It is only recently that computational studies of the OER mechanism on IrO_2 have started to appear, albeit mostly based on model surfaces in vacuum or with implicit solvation.[19–22] However, insights into the coupling between the reaction mechanism, activity and stability, are still limited, owing to a general lack of microscopic information on the IrO_2-water interface.[2,6,8,23–30]

The important role of the surface chemistry of IrO_x electrocatalysts in the OER[3] was recently demonstrated through a combination of experiments and computational studies. However, the roles of surface chemistry and applied voltage are highly interconnected, and separating the two is far from trivial.[31,32] Indeed this remains a major challenge in discerning the atomistic factors that control the kinetics of inner-sphere electron transfer processes encountered in heterogeneous electrocatalysis.[30,33] Therefore, it is highly relevant to characterize the surface proton affinities of the different surface sites and the resultant acid-base equilibria at the IrO_2-water interface in the absence of external fields and other perturbations.

One fundamental characteristic of oxide surfaces is the point of zero proton charge (pH_{PZC}), which controls the effective surface charge. At $p_H < pH_{PZC}$, the surface prefers to adsorb protons while at $p_H > pH_{PZC}$ the hydroxy group is preferred, thus directly affecting the adsorption of ions, surface composition of adsorbed species, and the surface reactivity as well.[31,34–36] Experimentally, this can be used as a tuning knob to optimize the OER kinetics through, e.g., the appropriate selection of electrolytes or via surface modification of the electrocatalyst.[25,30,37,38] However, central to the atomistic design and optimization of the electrocatalyst is the estimation of the acid dissociation constants (pK_as) of the different surface sites, which are directly related to the pH_{PZC} but still not accessible using current experimental techniques. Therefore, their estimation through computational methods provides critical information on how atomistic features can be used to influence macroscopic observables. In a broader context, the acid-base chemistry of metal-oxide water interfaces is also important in environmental geochemistry,[39–41] biomass conversion[42] and various other applications, and the surface composition of these complex interfaces can also be elucidated through the computational estimation of the pK_as of the different surface sites as done in this work.

In this work, we set out to elucidate the acid-base equilibrium at the rutile IrO_2-water interface, while also providing a detailed characterization of the hydration structure of this interface, hitherto unreported in the literature. To overcome the fundamental limitations of system size and timescales accessible through conventional AIMD simulations (especially cumbersome for water-metal interfaces such as aqueous IrO_2) we trained a deep neural network potential (DP) using accurate first-principles data to represent the potential energy surface of water in contact with the most abundant (110) surface of rutile IrO_2.[43] After validating the trained DP by its ability to reproduce the hydration structure obtained from a short AIMD simulation, a long (nanosecond) timescale equilibrium sampling of the interface using deep-potential molecular dynamics (DPMD) provided fundamental insights such as the water dissociation fraction and proton transfer mechanisms. We found that a significant fraction ($\approx 80\%$) of the adsorbed water was dissociated at the interface. However, the lifetime of the resulting terminal hydroxy groups was relatively short due to the prevalence of proton transfer mechanisms that preserved the dissociated fraction but caused rapid interchanges in the identity of the adsorbed species. These observations formed the basis for the subsequent simulations combining DPMD and enhanced sampling methods, which allowed an efficient exploration of the free-energy surface to obtain quantitative estimates of the pK_a of the different surface sites and the pH_{PZC}, found to agree well with experiments. The free-energy for water dissociation obtained from the computed pK_as was exergonic, consistent with the observed large water dissociation fraction. Overall, these results support a scenario where the commonly assumed rate-determining step in the OER may involve proton transfer between the surface sites, rather than across the double layer into solution.[3,38]

The DP for the $IrO_2(110)$-water interface was trained using the active-learning approach of Zhang *et al.*,[43,44] with first-principles data for the following systems and thermodynamic conditions: a) bulk IrO_2 (96 atoms) at 200-1000 K and 1 bar; b) isolated water molecules adsorbed on a (2×4) rutile $IrO_2(110)$ surface in vacuum (198 atoms) at 200-600 K and constant volume; c) (2×4) $IrO_2(110)$ interfaced with a 16 Å thick water layer (432 atoms) at 200-800 K and constant volume; and d) liquid water (192 atoms) at configurations taken from Ref.[34] For the calculation of the surface acidity, configurations obtained from enhanced sampling simulations, involving the (2×4) $IrO_2(110)$-water (16 Å) interface with a net non-zero proton charge on the IrO_2 surface and a free hydronium or hydroxide ion in solution, were also included as part of the training set. At the end of the training, three distinct DPs that differed only in their initialization were obtained. All computational details concerning the training procedure as well as the AIMD, DPMD and enhanced sampling simulations are given in the Supporting Information (SI).

As a first assessment of the quality of the DP, Figure S3 in SI shows the parity plot of the norm of the atomic forces (100 configurations), comparing the values given by the DP versus those computed using Density functional theory (DFT) with the SCAN[45] exchange-correlation functional, for each of the different systems used in the training. Root mean-square errors (RMSE) are in the range 130-180 meV/ Å, which is similar to that of previous DPMD studies of aqueous oxide interfaces[34,46,47] and suggests a well-trained DP model.

We also assessed the ability of the DP to describe configurations involving the $IrO_2(110)$ surface with a net non-zero proton charge and a free hydronium ion in water at distances lower and higher than the short-range cut-off (6 Å) used to define the atomic environments during training. As shown by the parity plots in Figure S4, the RMSE in atomic energy and forces are similar for the two cases, indicating that despite the lack of long-range electrostatics[48] the trained DP reproduces the DFT-SCAN results for proton transfer processes with good accuracy. This DP can thus be confidently used to study the acid-base equilibrium at the (2×4) IrO_2(110)-water (16 Å) interface (i.e., the model used for the training).

Additional validation tests included the bulk lattice constant of rutile IrO_2 (Table S6 in the SI), the dissociation barrier for a single water molecule adsorbed on (2×4) rutile IrO_2(110) in vacuum (Figure S5 in the SI), and the relative stabilities of different configurations of a water monolayer adsorbed on the same surface (Figure S6 in the SI). In particular, the DP well reproduces the DFT-SCAN prediction of almost barrier-less dissociation of molecular water adsorbed on the Ir_{cus} site to form a terminal hydroxy group (OH_{cus}) and a protonated O_{br} site. Similarly, both DFT-SCAN and the DP predict that the completely dissociated configuration of a monolayer of water is $\approx$ 0.35 eV/molecule more stable than the completely molecular configuration, with the partially dissociated configurations falling in between the two (Figure S6). The above results are also in agreement with prior computational studies.[11,12]

In order to evaluate the DP's ability to represent the potential energy surface of the IrO_2-water interface, we further compared the water density profiles and radial distribution functions (RDFs) of selected atom pairs obtained from 15 ps long AIMD and DPMD simulations of the (2×4) IrO_2(110)-water (16 Å) interface (Figure 1). Both DPMD and AIMD predict an almost symmetric water-density profile characterized by a sharp peak corresponding to the first adsorbed water-layer followed by a smaller peak corresponding to a layer of intact water molecules hydrogen bonded to the adsorbed water. In addition, DPMD well reproduces the RDFs of selected atom-pairs at the interface (Figure 1b). Specifically, the strong peak at ∼1 Å for the O_{br}-H_w RDF indicates a significant fraction of dissociated adsorbed water at the interface, resulting in largely protonated O_{br} sites (H_w is the water hydrogen atom; used interchangeably with D). Similarly, the first peak of the Ir_{cus}-O_w RDF at $\approx$2 Å is largely representative of adsorbed hydroxy groups (rather than molecular water), which are in turn hydrogen bonded to the next layer of intact water molecules (O_w is the water oxygen atom). This picture is confirmed by the

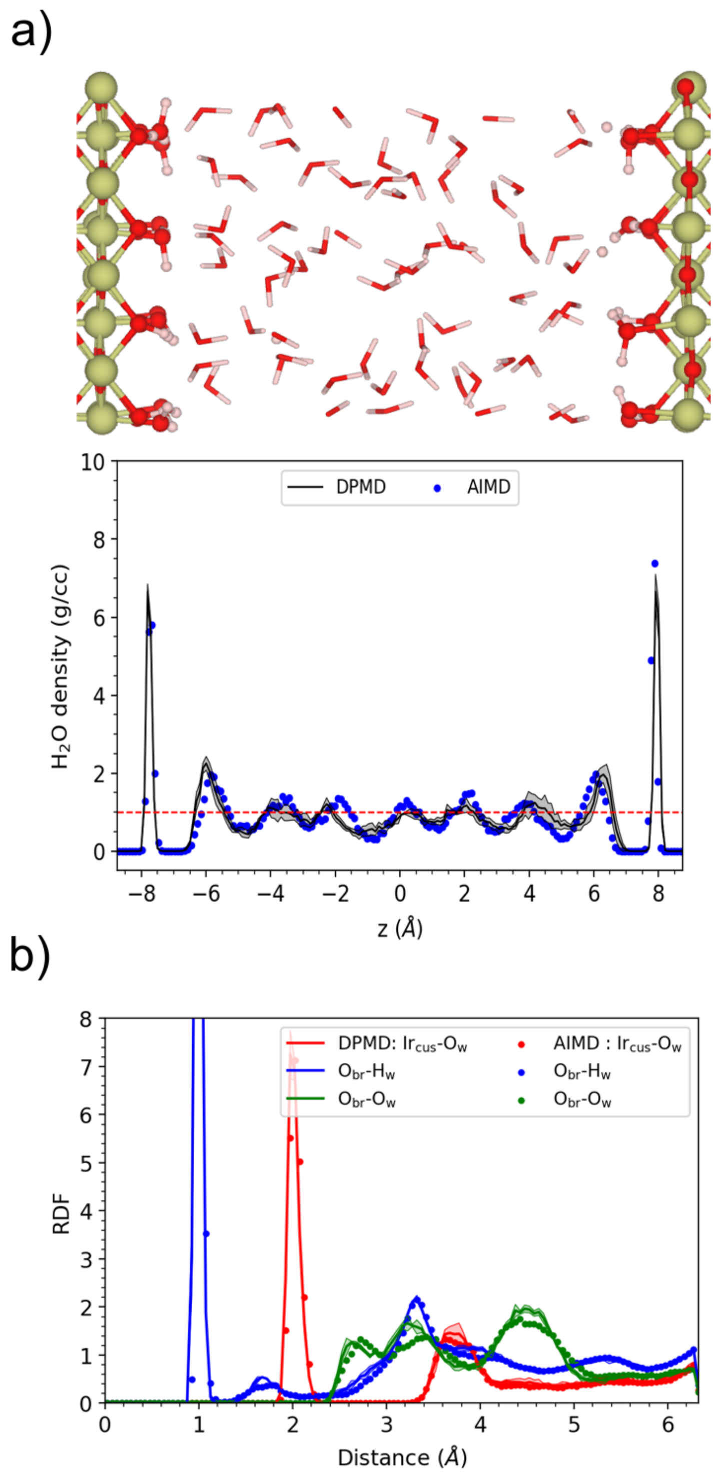

Figure 1: Comparison between results from 15 ps AIMD (symbols) and DPMD simulations for (2×4) rutile IrO_2(110) interfaced with water (16 Å): (a) water density profile and (b) radial distribution functions of selected atom pairs. The solid lines and shaded areas correspond to the average and standard deviation of three independent DPMD simulations, each run with a distinct DP. Color codes- Ir: gold, O: red, H: white.

vibrational density of states (vDOS) for the first (adsorbed) and second water layers, as shown in Figure S7a of the SI. Finally, the DP well reproduces the O_w-O_w RDF of liquid water obtained from AIMD (see Figure S9).

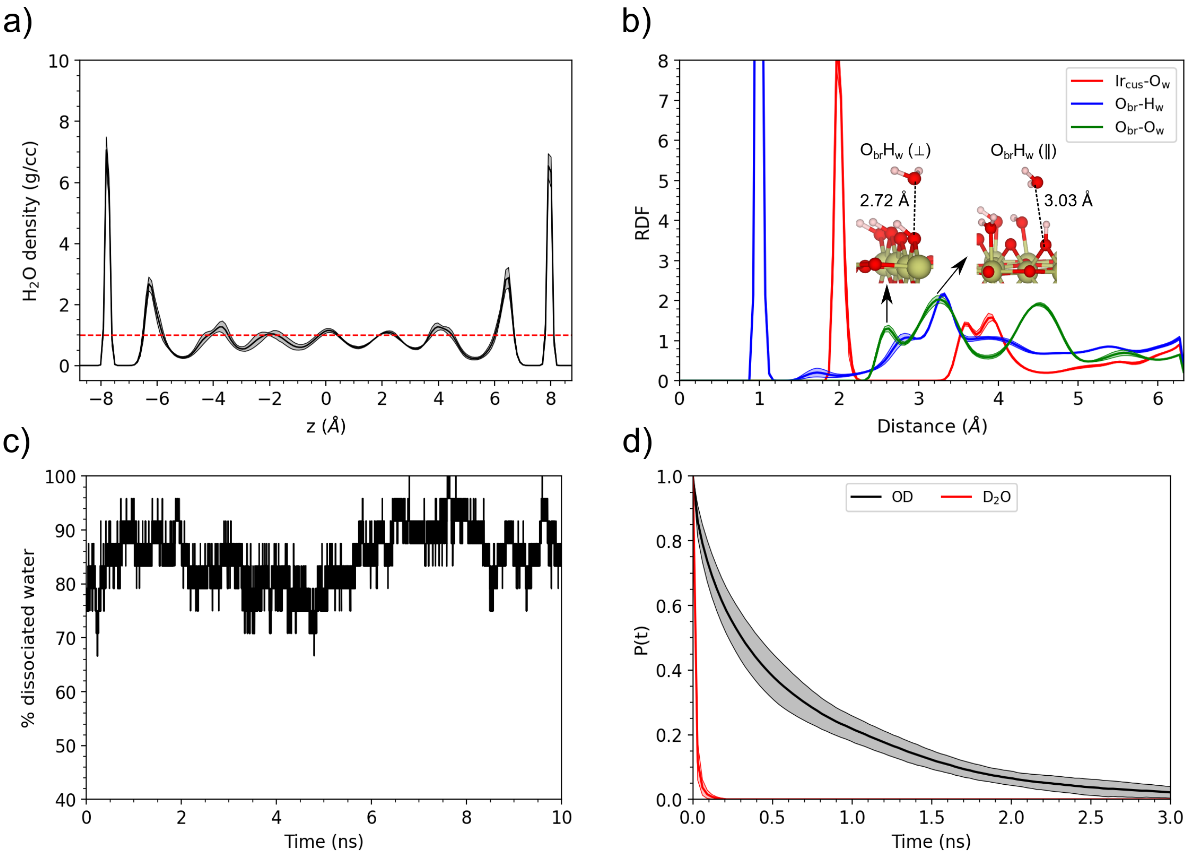

Figure 2: Results from 10 ns DPMD simulations of (2×4) rutile $IrO_2(110)$ interfaced with water (16 Å): a) water density profile (last 5 ns), b) radial distribution functions of selected pairs (last 5 ns), c) percentage of dissociated water on the Ir_{cus} sites and d) survival probability of OD/D_2O adsorbed on the Ir_{cus} sites. The solid lines and shaded areas correspond to the average and standard deviation of three independent DPMD simulations, each run with a distinct DP. The inset in b) illustrates the different orientations of the $O_{br}H_w$ bonds that affect the positions of the water molecules in the adjacent layer, represented by the double peaks in the O_{br}-O_w RDF.

The equilibrium structure of $IrO_2(110)$-water interface was characterized by performing 10 ns long DPMD simulations for three interface models: (2×4) $IrO_2(110)$ in contact with a 16 Å thick slab of water (model **I1**); (2×4) $IrO_2(110)$ interfaced with 30 Å water (model **I2**); and (4×8) $IrO_2(110)$ interfaced with 16 Å water (model **I3**). The hydration structures and water dissociation fractions of these systems are shown in Figures 2 (**I1**), S10 (**I2**) and S11 (**I3**). The interfacial water density profile is essentially identical for all three interface models, with the first sharp peak representing the adsorbed water-layer and the second peak corresponding to the second (intact) water layer, at ≈1.5 Å above the adsorbed one. The layering of the interfacial water molecules becomes more diffuse moving away from the IrO_2 surface, with the third water layer represented by an even smaller peak at ≈2.5 Å above the second layer. The effect of confinement between the periodic interfaces does not manifest in the density profile at the interface, but rather in the bulk water region, where the oscillations in the water density around 1g/cm^3 vanish for the 30 Å thick water layer (model **I2**). It is also interesting to consider the hydrogen bond structure at the interface, which is illustrated by the hydrogen atom density profile in Figure S12. One can see hydrogen bonds between the different water layers, especially prominent between the first two layers.

The radial distribution functions of selected atomic pairs for the different interface models are also identical (see Figures 2b, S10b and S11b for **I1**, **I2** and **I3**, respectively), and similar to those shown in Figure 1b. Since models **I2** and **I3** were not part of the training set, the consistency of their properties with those of model **I1** is an indication of the robustness of the DP model in its application towards larger system sizes. These RDFs confirm the significant amount of dissociated water at the interface, as evidenced by the first-peak of the O_{br}-H_w RDF. Another interesting feature is the double peak of both the O_{br}-O_w and the O_{br}-H_w RDFs around ≈ 3 Å. This can be understood by considering the distribution of the angles between the O_{br}-H_w bonds of the dissociated adsorbed water layer and the surface normal (see Figure S13), which shows the presence of both O_{br}-$H_w(\perp)$ and O_{br}-$H_w(\|)$ species (i.e., surface bridging hydroxy groups perpendicular and parallel to the surface normal) at the interface. This distribution directly influences the positions of the water molecules in the layer above. Molecules interacting with the O_{br}-$H_w(\perp)$ species are indeed closer to the surface than those interacting with the O_{br}-$H_w(\|)$ species (see inset of Figure 2b), which explains the double peak in the O_{br}-O_w RDF.

The significant extent of dissociation is quantified in Figure 2c, which shows the time evolution of the percentage of dissociated water molecules adsorbed at the Ir_{cus} site (see Figures S10c and S11c in the SI for dissociation in models **I2** and **I3**). The average dissociation fraction is ≈ 80% for all three interface models (Table 1), confirming the strong preference for water to be adsorbed in dissociated form on $IrO_2(110)$. In addition, the survival probabilities, $P(t)$, plotted in Figure 2d, show a much faster decay for adsorbed molecular water (D_2O) on the Ir_{cus} sites in comparison to dissociated water (OD) (see Figures S10d and S11d in the SI for **I2** and **I3**). The average lifetime, computed as: $\tau = \int_0^\infty P(t)tdt / \int_0^\infty P(t)dt$, is indeed an order of magnitude larger for dissociated vs molecular water (see Table 1). However, τ_{OD} is quite small considering the large dissociation fraction of $\approx$ 80% in our simulations. (For comparison, $\tau_{OD} \sim 0.6$ ns has been reported for anatase $TiO_2(101)$, but the average water dissociation fraction was only $\sim$ 6% for that surface.[34]) This suggests a rapid inter-conversion among the OD's adsorbed on different Ir_{cus} sites, an effect that may play a crucial role in the rate-determining step of the OER,[3,38] and is discussed further after the description of the acid-base equilibrium of the aqueous rutile $IrO_2(110)$ interface.

Table 1: Average dissociation fraction of water, and average lifetimes of D_2O and OD adsorbed on the Ir_{cus} sites, obtained from DPMD simulations of models I1, I2 and I3 of the rutile $IrO_2(110)$-water interface.

System	Dissociation fraction (%)	τ_{D_2O} (ps)	τ_{OD} (ps)
I1	83.4 ± 5.5	12 ± 6	725 ± 63
I2	78.1 ± 4.8	11 ± 4	320 ± 112
I3	81.6 ± 2.4	13 ± 3	517 ± 25

To elucidate the mechanisms of proton transfer, it is essential to unambiguously identify the protonation states of the Ir_{cus} and O_{br} surface sites during the equilibrium simulations. For this purpose, we used the protonation state collective variable (CV) s_p introduced in Ref.[49] , which is based on a partition of the space into Voronoi polyhedra. A detailed description of this CV (also used for the enhanced sampling simulations reported below) is given in Refs.[49,50] and its utilization in the present context is elaborated in the SI (see Table S8).

Figure 3a shows the time evolution of s_p for the Ir_{cus} (black line) and O_{br} (red line) sites, as well as their sum describing the net protonation state of the surface (blue line), during a DPMD simulation with one of the three independent DPs for model **I1** (see Figures S14a and b in the SI for the other DPs and models). A prominent feature in Figure 3a is that the net protonation state of the surface is zero, indicating a charge

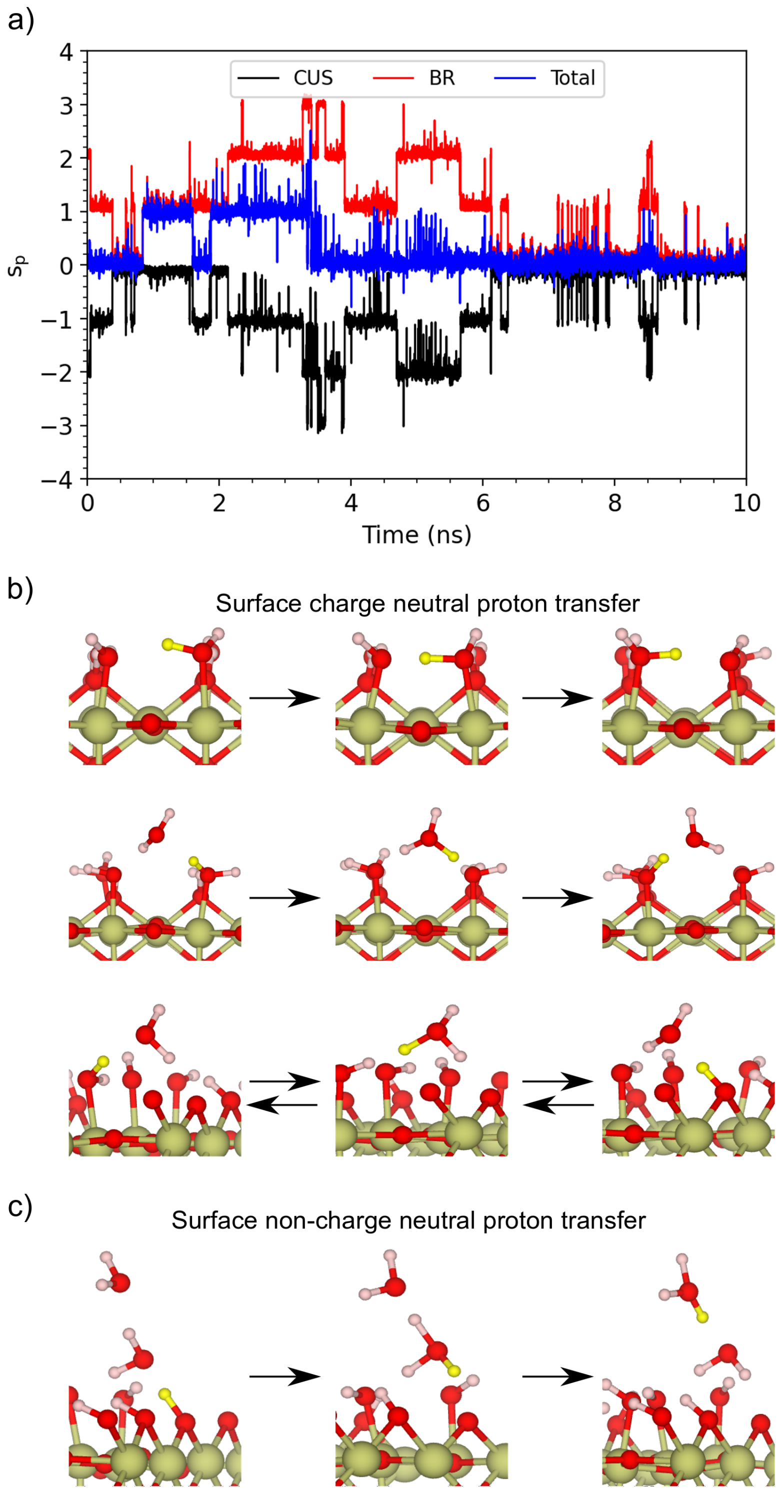

Figure 3: Protonation states and proton transfer mechanisms from equilibrium DPMD simulations of (2×4) rutile $IrO_2(110)$ interfaced with water (16 Å): a) protonation states of the Ir_{cus} and O_{br} sites and net surface protonation state, as obtained from one of three independent DPs; b) pathways of surface charge-neutral proton transfer and c) observed pathway for the surface non-charge-neutral proton transfer. Color codes-Ir: gold, O: red, H: white; the proton being transferred is highlighted in yellow.

neutral surface, for most of the simulation, despite frequent changes in the values of the individual s_p's for the Ir_{cus} and O_{br} sites. However, there are also relatively short periods where the surface acquires a net non-zero charge. On closer inspection, we find that a charge neutral surface occurs when there is either no proton transfer, or proton transfer between the OH/H_2O adsorbed on the Ir_{cus} sites or else from H_2O adsorbed on the Ir_{cus} site to the O_{br} site (dissociation of adsorbed water) and vice-versa. On the other hand, release or uptake of a proton from water results in the surface acquiring a net non-zero charge, with either a solvated H_3O^+ or OH^- in solution.

In more detail, the different modes of proton transfer at the rutile IrO_2(110)-water interface observed in our simulations are illustrated in Figures 3b and c. Three distinct modes of proton transfer that preserve surface charge neutrality were observed, namely: a) direct proton transfer between adsorbed H_2O and OH on adjacent Ir_{cus} sites (Figure 3b top), b) second layer water-assisted proton transfer between adsorbed H_2O and OH on adjacent Ir_{cus} sites (Figure 3b middle) and c) second layer water-assisted dissociation of adsorbed H_2O on the Ir_{cus} site to form OH_{cus} and OH_{br}, and the reverse of this process (Figure 3b bottom). We note that, in contrast to c), mechanisms a) and b) do not change the total dissociated fraction of adsorbed water, although the identity of the adsorbed species changes rapidly between H_2O and OH. A prevalence of such mechanisms can thus explain the rapid decorrelation of the adsorbate identity resulting in small survival probability reported in Figure 2d.

The most common type of proton transfer leading to a loss of surface charge neutrality is shown in Figure 3c. In this process, the OH_{br} releases its proton to water resulting in the formation of a net negative charge on the surface, and a solvated H_3O^+ species in solution. This process is rarely observed over the course of a 10 ns simulation, suggesting the existence of a finite free-energy barrier for this proton transfer to occur. Nevertheless, it points to the acidic character of the aqueous rutile IrO_2(110) interface, as observed in experiment.[51]

The acid-base equilibrium of oxide surfaces is a complex process, involving various interconnected steps and rare-events such as proton dissociation and transfer.[32] The method of choice for calculating the pH_{PZC}, especially for oxides where proton transfer between the surface sites is infrequent, has been free-energy perturbation (FEP),[31,35,36,52] but extension of this method to interfaces that involve rapid proton exchanges between the surface sites is not straightforward.[36] In this study, we thus use an approach based on enhanced sampling, notably well-tempered metadynamics combined with appropriately chosen CV's and DPMD, to estimate the acidity of aqueous IrO_2.

Following the method of Grifoni *et al.*,[49] we used two CV's, namely s_p that describes the protonation state and s_d that measures the distance between the pair of atoms that have exchanged protons, for each of the two different reactive surface sites (Ir_{cus} and O_{br}). Taking the fully hydroxylated surface as the reference state in each case, we studied the release of a proton from OH_{br}^+ to form H_3O^+, i.e.,

$OH_{br}^+ \ + \ H_2O(l) \ \rightarrow \ O_{br} \ + \ H_3O^+(aq),$

and the uptake of a proton from neutral water to any of the OH_{cus}^-, i.e.,

$OH_{cus}^- \ + \ H_2O(l) \ \rightarrow \ H_2O_{cus} \ + \ OH^-(aq),$

separately. The implementation of the CV's for this system along with all other details of the enhanced sampling simulations are provided in the SI (see Table S5).

The converged free-energy surfaces (FES) for the deprotonation of the OH_{br}^+ site and the protonation of the OH_{cus}^- site are shown in Figure 4a and b respectively (see Figure S15 in the SI for the evolution of the s_p CV over the course of the simulation). We observed that the OH_{br}^+ transfers its proton to the nearest water molecule to form a hydronium ion (H_3O^+), while subsequent proton transfer into solution happens through the Grotthus mechanism. Similarly, release of a proton to an OH_{cus}^- site by the nearest water molecule results in an adsorbed H_2O_{cus} and a free hydroxide ion (OH^-) in solution. With the release of a proton, the surface acquires a net negative charge, while it is positively charged in the latter case.

The free-energy for deprotonation/protonation (ΔF) can be directly estimated from the converged FES, resulting in 20.4 $\pm$ 2.3 kJ/mol for the deprotonation of OH_{br}^+, and 61.8 $\pm$ 5.2 kJ/mol for the protonation of OH_{cus}^-. The pK_a for the O_{br} site can be

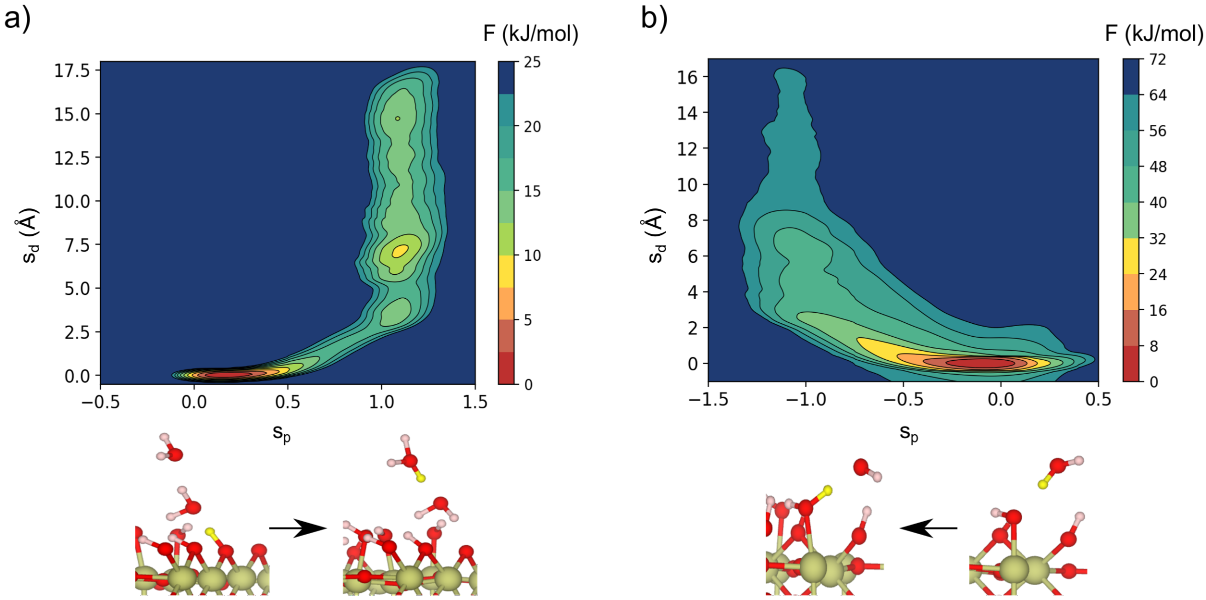

Figure 4: The free-energy surface for a) deprotonation of the OH^+_{br} site ($OH^+_{br} \rightarrow H_3O^+$) and b) protonation of the OH^-_{cus} site ($OH^-_{cus} \rightarrow H_2O_{cus}$), from DPMD enahanced sampling simulations of the (2×4) IrO_2(110)-water (16 Å) interface. The bottom panels show a sketch of the proton transfer process for each case. Color code: Ir, gold; O, red; H, white (the proton being transferred is highlighted in yellow). The free-energy surface is obtained from the average of three independent DPMD simulations each run with a different DP. We also note that the distance between the periodic interfaces is ≈18 Å , while the water slab is 16 Å thick. This accounts for the values of the s_d CV >16 Å in a) since it measures the distance of a proton transferred from a O_{br} site to water.

estimated from the free-energy for deprotonation ($pK_a = \Delta F/2.303k_BT$), resulting in $pK_{a,br} = 3.6 \pm 0.4$. Since the formal definition of Brønsted acidity is based on the release of protons, the $pK_{a,cus}$ for the Ir_{cus} site is obtained from the corresponding $pK_{b,cus}$ (estimated from the ΔF for protonation) and the water ionic product pK_W, that is $pK_{a,cus} = pK_W - pK_{b,cus}$. To be fully consistent, the pK_W should also be computed using our DP water model, but here we simply take the experimental value of the pK_W (14.0[53]), while also considering the sensitivity of the pH_{PZC} and the dissociation free energy ΔF_{diss} (defined below) to changes of ± 0.5 of this value (see Table S9). This gives $pK_{a,cus} = 3.2 \pm 0.9$, implying a significant acidity of the aqueous IrO_2(110) surface.

Using the pK_a's of the individual surface sites, the pH_{PZC} is given by $pH_{PZC} = (pK_{a,br} + pK_{a,cus})/2 = 3.4 \pm 0.6$, in good agreement with the experimental estimate of ≈ 3.[51] The free-energy for the dissociation of a water molecule adsorbed on the Ir_{cus} site can also be estimated from the pK_a's of the two sites,[31] which gives $\Delta F_{diss} =$

$2.303k_BT[pK_{a,cus} - pK_{a,br}] = -1.8 \pm 4.9$ kJ/mol. We note that although ΔF_{diss} is highly sensitive to the choice of pK_W, varying from -4.7 to +1.0 kJ/mol for pK_W in the range 13.5 to 14.5, its value always suggests that water dissociation is facile, as observed in our equilibrium DPMD simulations. To quantify the fraction of water dissociation, we assume a simple two state model, such that the probability of adsorbed water being dissociated (P_{diss}) is given by $P_{diss} = e^{-\beta\Delta F_{diss}}/(1+e^{-\beta\Delta F_{diss}})$. This results in an average dissociation fraction of ≈68%, in reasonable agreement with the value observed in the equilibrium sampling simulation (≈83%). This further validates both the acidic nature of the interface, as well as its equilibrium surface composition. Finally, the estimation of the pK_a's of the different surface sites also allows the determination of the fraction of sites that are protonated or occupied by hydroxy groups as a function of pH (see Figure S16), which for a metal oxide holds significance across many different applications including electrocatalysis.[35]

We note that the mechanisms of proton transfer and the significant Brønsted acidity of the IrO_2(110) surface revealed by our simulations may play a crucial role in the OER. In particular, the formation of the OOH^*_{cus} intermediate commonly thought to be the rate-determining step[3,33] may proceed through proton transfer between adjacent Ir_{cus} sites (i.e., $2\ O^*_{cus} + H_2O \rightarrow OOH^*_{cus} + OH^*_{cus}$) or between Ir_{cus} and O_{br} sites (i.e., $O^*_{cus} + O^*_{br} + H_2O \rightarrow OOH^*_{cus} + OH^*_{br}$) without the formal transfer of a proton into solution. This mechanism is highly compatible with the facile dissociation of H_2O_{cus} via proton transfer to the O_{br} site, as well as the rapid exchange of protons between OH_{cus} and H_2O_{cus} seen in our simulations (see Figure 3). In such a scenario, the rate-determining step would depend on the concentration of oxidized surface sites from the subsequent deprotonation of either OH^*_{cus} or OH^*_{br}, as suggested by recent experiments.[3] Indeed, such a scenario involving the "chemical transfer" of protons between different surface sites by modulating their Brønsted acidity has been suggested for the improved performance observed in Ru-W binary oxides.[38] Importantly, the Tafel slope was found to be 42 mV dec^{-1},[38] nearly identical to the 43-47 mV dec^{-1} slope for crystalline IrO_2,[3] suggesting the possible existence of a general OER mechanism for metal oxides with strong Brønsted acidity and rapid proton transfer between different surface sites. Therefore, a careful analysis of the acid-base equilibrium and quantitative estimates of the pK_a's of the different surface sites provide a potential route to uncover important molecular factors that control macroscopic observables.

In summary, we have reported *ab-initio* based neural network potential simulations that provide a comprehensive picture of the hydration structure, proton transfer mechanism and acid-base equilibrium on aqueous rutile $IrO_2(110)$, a model electrocatalytic interface. Our results show that this interface is characterized by a large fraction of dissociated water, with rapid proton exchanges between the different surface sites that preserve the net surface charge. In rare instances, the release of a proton from a surface O_{br} site to water is also observed, resulting in a net negative surface charge and a solvated hydronium ion, revealing the acidic nature of the interface. Enhanced sampling simulations provide accurate estimates of the pK_a's of the different surface sites and a pH_{PZC} of ≈ 3.4, in excellent agreement with experiments. The obtained estimate for the free-energy of water dissociation indicates that this reaction is exergonic, confirming the equilibrium surface composition and the observed acid-base equilibrium at the interface. The predicted short lifetime of the terminal hydroxy groups as a result of rapid proton exchange and the strong Brønsted acidity of the surface sites suggest that the rate-determining step in the OER may involve "intramolecular" proton transfer, with the concentration of oxidized sites formed by deprotonation of OH_{cus} and OH_{br} sites largely determining the overall rate, as shown by Tafel analysis in recent experiments.[3,38] The present results therefore lay the foundation for a systematic investigation of the structure of the electrical double layer and its influence on the surface reactivity of electrocatalysts.

Supporting Information

Computational methods, DP validation, and results from DPMD simulations (equilibrium sampling and enhanced sampling). Figure S1: Dependence on FFT grids; Figure

S2: Atomic structure of surface super-cell; Figure S3,S4: Parity plot of forces and energy for charge neutral and non-charge neutral surfaces; Figure S5: DP validation for dissociation of single adsorbed water; Figure S6: DP validation for relative energies of different configurations of a monolayer of adsorbed water; Figure S7: vDOS comparison between DPMD and AIMD of water layers; Figure S8: vDOS comparison between DPMD and AIMD for IrO_2 slab; Figure S9: Water RDF comparison between DPMD and AIMD; Figure S10: Hydration structure of interface model **I2**; Figure S11:Hydration structure of interface model **I3**; Figure S12: Oxygen and hydrogen density profiles for interface models **I1** and **I2**; Figure S13: Angle distributions of the OH_{cus} and OH_{br} bonds; Figure S14: Protonation state of interface models **I1** and **I2**; Figure S15: Evolution of the s_p CV; Figure S16: Surface composition as a function of pH; Table S1: Surface energy vs number of layers; Table S2: Surface energy vs k-point grid; Table S3: Atomic force vs k-point grid; Table S4: Adsorption energy of water; Table S5: Parameters used in the well-tempered metadynamics; Table S6: Validation of lattice constants; Table S7: Lateral diffusion coefficient of interfacial water; Table S8: Possible surface protonation states; and Table S9: Deprotonation/Protonation free-energy, pK_a and pH_{PZC}.

Acknowledgments

This work was supported by DoE BES, CSGB Division under Award DESC0007347, with further support from the Computational Chemical Center: Chemistry in Solution and at Interfaces, funded by DoE under Award DESC0019394. The authors acknowledge the use of computational resources (Stampede2 at TACC) provided by the Extreme Science and Engineering Discovery Environment (XSEDE) supported though the National Science Foundation (NSF) under award number CHE210079, and the National Energy Research Scientific Computing Center (NERSC), under DoE Contract No. DE-AC02-05cH11231. We also acknowledge the use of the Princeton Research Computing resources at Princeton University which is a consortium of groups led by the Princeton Institute for Computational Science and Engineering (PICSciE) and Office of Information

Technology's Research Computing.

References

(1) Seh, Z. W.; Kibsgaard, J.; Dickens, C. F.; Chorkendorff, I.; Nørskov, J. K.; Jaramillo, T. F. Combining theory and experiment in electrocatalysis: Insights into materials design. *Science* **2017**, *355*, eaad4998.

(2) Lončar, A.; Escalera-López, D.; Cherevko, S.; Hodnik, N. Inter-relationships between oxygen evolution and iridium dissolution mechanisms. *Angew. Chem. Int. Ed.* **2022**, *61*, e202114437.

(3) Nhan Nong, H.; Falling, L. J.; Bergmann, A.; Klingenhof, M.; Phi Tran, H.; Spöri, C.; Mom, R.; Timoshenko, J.; Zichittella, G.; Knop-Gericke, A. et al. Key role of chemistry versus bias in electrocatalytic oxygen evolution. *Nature* **2020**, *587*, 408–413.

(4) Cherevko, S. Stability and dissolution of electrocatalysts: Building the bridge between model and "real world" systems. *Curr. Opin. Electrochem.* **2018**, *8*, 118–125.

(5) Chen, F.-Y.; Wu, Z.-Y.; Adler, Z.; Wang, H. Stability challenges of electrocatalytic oxygen evolution reaction: From mechanistic understanding to reactor design. *Joule* **2021**, *5*, 1704–1731.

(6) Cherevko, S.; Reier, T.; Zeradjanin, A. R.; Pawolek, Z.; Strasser, P.; Mayrhofer, K. J. Stability of nanostructured iridium oxide electrocatalysts during oxygen evolution reaction in acidic environment. *Electrochem. Commun.* **2014**, *48*, 81–85.

(7) Over, H. Fundamental studies of planar single-crystalline oxide model electrodes (RuO_2, IrO_2) for acidic water splitting. *ACS Catal.* **2021**, *11*, 8848–8871.

(8) Knöppel, J.; Möckl, M.; Escalera-López, D.; Stojanovski, K.; Bierling, M.; Böhm, T.; Thiele, S.; Rzepka, M.; Cherevko, S. On the limitations in assessing stability of

oxygen evolution catalysts using aqueous model electrochemical cells. *Nat. Commun.* **2021**, *12*, 1–9.

(9) Man, I. C.; Su, H. Y.; Calle-Vallejo, F.; Hansen, H. A.; Martínez, J. I.; Inoglu, N. G.; Kitchin, J.; Jaramillo, T. F.; Nørskov, J. K.; Rossmeisl, J. Universality in oxygen evolution electrocatalysis on oxide surfaces. *ChemCatChem* **2011**, *3*, 1159–1165.

(10) Pittkowski, R.; Krtil, P.; Rossmeisl, J. Rationality in the new oxygen evolution catalyst development. *Curr. Opin. Electrochem.* **2018**, *12*, 218–224.

(11) Siahrostami, S.; Vojvodic, A. Influence of adsorbed water on the oxygen evolution reaction on oxides. *J. Phys. Chem. C* **2015**, *119*, 1032–1037.

(12) Gauthier, J. A.; Dickens, C. F.; Chen, L. D.; Doyle, A. D.; Nørskov, J. K. Solvation effects for oxygen evolution reaction catalysis on IrO_2(110). *J. Phys. Chem. C* **2017**, *121*, 11455–11463.

(13) Zhao, F.; Wen, B.; Niu, W.; Chen, Z.; Yan, C.; Selloni, A.; Tully, C. G.; Yang, X.; Koel, B. E. Increasing iridium oxide activity for the oxygen evolution reaction with hafnium modification. *J. Am. Chem. Soc.* **2021**, *143*, 15616–15623.

(14) Wang, Y.; Zhang, L.; Yin, K.; Zhang, J.; Gao, H.; Liu, N.; Peng, Z.; Zhang, Z. Nanoporous iridium-based alloy nanowires as highly efficient electrocatalysts toward acidic oxygen evolution reaction. *ACS Appl. Mater. Interfaces* **2019**, *11*, 39728–39736.

(15) Godínez-Salomón, F.; Albiter, L.; Alia, S. M.; Pivovar, B. S.; Camacho-Forero, L. E.; Balbuena, P. B.; Mendoza-Cruz, R.; Arellano-Jimenez, M. J.; Rhodes, C. P. Self-supported hydrous iridium-nickel oxide two-dimensional nanoframes for high activity oxygen evolution electrocatalysts. *ACS Catal.* **2018**, *8*, 10498–10520.

(16) Alia, S. M.; Shulda, S.; Ngo, C.; Pylypenko, S.; Pivovar, B. S. Iridium-based nanowires as highly active, oxygen evolution reaction electrocatalysts. *ACS Catal.* **2018**, *8*, 2111–2120.

(17) Guo, H.; Fang, Z.; Li, H.; Fernandez, D.; Henkelman, G.; Humphrey, S. M.; Yu, G. Rational design of rhodium-iridium alloy nanoparticles as highly active catalysts for acidic oxygen evolution. *ACS Nano* **2019**, *13*, 13225–13234.

(18) Kim, Y. T.; Lopes, P. P.; Park, S. A.; Lee, A. Y.; Lim, J.; Lee, H.; Back, S.; Jung, Y.; Danilovic, N.; Stamenkovic, V. et al. Balancing activity, stability and conductivity of nanoporous core-shell iridium/iridium oxide oxygen evolution catalysts. *Nat. Commun.* **2017**, *8*, 1–8.

(19) Ping, Y.; Nielsen, R. J.; Goddard, W. A. I. The reaction mechanism with free energy barriers at constant potentials for the oxygen evolution reaction at the IrO_2 (110) surface. *J. Am. Chem. Soc.* **2017**, *139*, 149–155.

(20) Klyukin, K.; Zagalskaya, A.; Alexandrov, V. Ab Initio thermodynamics of iridium surface oxidation and oxygen evolution reaction. *J. Phys. Chem. C* **2018**, *122*, 29350–29358.

(21) Zagalskaya, A.; Alexandrov, V. Role of defects in the interplay between adsorbate evolving and lattice oxygen mechanisms of oxygen evolution reaction in RuO_2 and IrO_2. *ACS Catal.* **2020**, *10*, 3650–3657.

(22) Opalka, D.; Scheurer, C.; Reuter, K. Ab initio thermodynamics insight into the structural evolution of working IrO_2 catalysts in proton-exchange membrane electrolyzers. *ACS Catal.* **2019**, *9*, 4944–4950.

(23) Zagalskaya, A.; Alexandrov, V. Mechanistic study of IrO_2 dissolution during the electrocatalytic oxygen evolution reaction. *J. Phys. Chem. Lett.* **2020**, *11*, 2695–2700.

(24) Raman, A. S.; Vojvodic, A. Providing atomistic insights into the dissolution of rutile oxides in electrocatalytic water splitting. *J. Phys. Chem. C* **2022**, *126*, 922–932.

(25) Kuo, D. Y.; Kawasaki, J. K.; Nelson, J. N.; Kloppenburg, J.; Hautier, G.; Shen, K. M.; Schlom, D. G.; Suntivich, J. Influence of surface adsorption on the oxygen evolution reaction on IrO_2(110). *J. Am. Chem. Soc.* **2017**, *139*, 3473–3479.

(26) Cherevko, S.; Geiger, S.; Kasian, O.; Kulyk, N.; Grote, J. P.; Savan, A.; Shrestha, B. R.; Merzlikin, S.; Breitbach, B.; Ludwig, A. et al. Oxygen and hydrogen evolution reactions on Ru, RuO_2, Ir, and IrO_2 thin film electrodes in acidic and alkaline electrolytes: A comparative study on activity and stability. *Catal. Today* **2016**, *262*, 170–180.

(27) Kasian, O.; Grote, J.-P.; Geiger, S.; Cherevko, S.; Mayrhofer, K. J. J. The common intermediates of oxygen evolution and dissolution reactions during water electrolysis on iridium. *Angew. Chem. Int. Ed.* **2018**, *57*, 2488–2491.

(28) Escudero-Escribano, M.; Pedersen, A. F.; Paoli, E. A.; Frydendal, R.; Friebel, D.; Malacrida, P.; Rossmeisl, J.; Stephens, I. E. L.; Chorkendorff, I. Importance of surface IrOx in stabilizing RuO_2 for oxygen evolution. *J. Phys. Chem. B* **2018**, *122*, 947–955.

(29) Mom, R. V.; Falling, L. J.; Kasian, O.; Algara-Siller, G.; Teschner, D.; Crabtree, R. H.; Knop-Gericke, A.; Mayrhofer, K. J. J.; Jesus Velasco-Vélez, J.-J.; Jones, T. E. Operando structure–activity–stability relationship of iridium oxides during the oxygen evolution reaction. *ACS Catal.* **2022**, *12*, 5174–5184.

(30) Zhang, R.; Pearce, P. E.; Duan, Y.; Dubouis, N.; Marchandier, T.; Grimaud, A. The importance of water structure and catalyst-electrolyte interface on the design of water splitting catalysts. *Chem. Mater.* **2019**, *31*, 8248–8259.

(31) Cheng, J.; Sprik, M. Acidity of the aqueous rutile TiO_2 (110) surface from density functional theory based molecular dynamics. *J. Chem. Theory Comput.* **2010**, *2*, 880–889.

(32) Rousseau, R.; Glezakou, V. A.; Selloni, A. Theoretical insights into the surface physics and chemistry of redox-active oxides. *Nat. Rev. Mater.* **2020**, *5*, 460–475.

(33) Boettcher, S. W.; Surendranath, Y. Heterogeneous electrocatalysis goes chemical. *Nat. Catal.* **2021**, *4*, 4–5.

(34) Andrade, M. F.; Ko, H. Y.; Zhang, L.; Car, R.; Selloni, A. Free energy of proton transfer at the water-TiO_2 interface from ab initio deep potential molecular dynamics. *Chem. Sci.* **2020**, *11*, 2335–2341.

(35) Di Liberto, G.; Maleki, F.; Pacchioni, G. pH dependence of MgO, TiO_2, and γ-Al_2O_3 surface chemistry from first principles. *J. Phys. Chem. C* **2022**, *126*, 10216–10223.

(36) Jia, M.; Zhang, C.; Cox, S. J.; Sprik, M.; Cheng, J. Computing surface acidity constants of proton hopping groups from density functional theory-based molecular dynamics: Application to the $SnO_2(110)/H_2O$ interface. *J. Chem. Theory Comput.* **2020**, *16*, 6520–6527.

(37) Giordano, L.; Han, B.; Risch, M.; Hong, W. T.; Rao, R. R.; Stoerzinger, K. A.; Shao-Horn, Y. pH dependence of OER activity of oxides: Current and future perspectives. *Catal. Today* **2016**, *262*, 2–10.

(38) Wen, Y.; Liu, C.; Huang, R.; Zhang, H.; Li, X.; García de Arquer, F. P.; Liu, Z.; Li, Y.; Zhang, B. Introducing Brønsted acid sites to accelerate the bridging-oxygen-assisted deprotonation in acidic water oxidation. *Nat. Commun.* **2022**, *13*, 4871.

(39) Wang, R.; Klein, M. L.; Carnevale, V.; Borguet, E. Investigations of water/oxide interfaces by molecular dynamics simulations. *Wiley Interdiscip. Rev. Comput. Mol. Sci.* **2021**, *11*, 1–26.

(40) Backus, E. H.; Schaefer, J.; Bonn, M. Probing the mineral-water interface with nonlinear optical spectroscopy. *Angew. Chem. Int. Ed.* **2021**, *60*, 10482–10501.

(41) Abdolhosseini Qomi, M. J.; Miller, Q. R.; Zare, S.; Schaef, H. T.; Kaszuba, J. P.; Rosso, K. M. Molecular-scale mechanisms of CO_2 mineralization in nanoscale interfacial water films. *Nat. Rev. Chem.* **2022**, *6*, 598–613.

(42) Védrine, J. C. Metal oxides in heterogeneous oxidation catalysis: State of the art and challenges for a more sustainable world. *ChemSusChem* **2019**, *12*, 577–588.

(43) Zhang, L.; Han, J.; Wang, H.; Car, R.; E, W. Deep potential molecular dynamics: A scalable model with the accuracy of quantum mechanics. *Phys. Rev. Lett.* **2018**, *120*, 143001.

(44) Zhang, L.; Lin, D.-Y.; Wang, H.; Car, R.; E, W. Active learning of uniformly accurate interatomic potentials for materials simulation. *Phys. Rev. Mater.* **2019**, *3*, 023804.

(45) Sun, J.; Ruzsinszky, A.; Perdew, J. Strongly constrained and appropriately normed semilocal density functional. *Phys. Rev. Lett.* **2015**, *115*, 036402.

(46) Schran, C.; Thiemann, F. L.; Rowe, P.; Müller, E. A.; Marsalek, O.; Michaelides, A. Machine learning potentials for complex aqueous systems made simple. *Proc. Natl. Acad. Sci. U.S.A* **2021**, *118*, e2110077118.

(47) Wen, B.; Calegari Andrade, M. F.; Liu, L.-M.; Selloni, A. Water dissociation at the water–rutile TiO_2 (110) interface from ab initio-based deep neural network simulations. *Proc. Natl. Acad. Sci. U.S.A* **2023**, *120*, e2212250120.

(48) Zhang, L.; Wang, H.; Muniz, M. C.; Panagiotopoulos, A. Z.; Car, R.; E, W. A deep potential model with long-range electrostatic interactions. *J. Chem. Phys.* **2022**, *156*, 124107.

(49) Grifoni, E.; Piccini, G.; Parrinello, M. Microscopic description of acid–base equilibrium. *Proc. Natl. Acad. Sci. U.S.A* **2019**, *116*, 4054–4057.

(50) Grifoni, E.; Piccini, G. M.; Lercher, J. A.; Glezakou, V. A.; Rousseau, R.; Parrinello, M. Confinement effects and acid strength in zeolites. *Nat. Commun.* **2021**, *12*, 2630–2639.

(51) Kosmulski, M. Isoelectric points and points of zero charge of metal (hydr)oxides: 50 years after Parks' review. *Adv. Colloid Interface Sci.* **2016**, *238*, 1–61.

(52) Ambrosio, F.; Wiktor, J.; Pasquarello, A. pH-dependent surface chemistry from

first principles: application to the $BiVO_4$(010)-water interface. *ACS Appl. Mater. Interfaces* **2018**, *10*, 10011–10021.

(53) Cheng, J.; Liu, X.; VandeVondele, J.; Sulpizi, M.; Sprik, M. Redox potentials and acidity constants from density functional theory based molecular dynamics. *Acc. Chem. Res.* **2014**, *47*, 3522–3529.